Received: 1 June 2023 | Revised: 20 October 2023 | Accepted: 22 October 2023

DOI: 10.1002/asna.20230094

Astronomische Nachrichten

ORIGINAL ARTICLE

Decomposition of the central structure of NGC 2273 in the NIR: A case study

L. Schey[1] | J. Heidt[1] | A. Pramskiy[1] | D. Thompson[2] | G. Agapito[3] | S. Esposito[3] | R. Gredel[4] | D. Miller[2] | E. Pinna[3] | A. Puglisi[3] | F. Rossi[3] | W. Seifert[1] | G. Taylor[3] | A. Quirrenbach[1]

[1]Landessternwarte, Zentrum für Astronomie der Universität Heidelberg, Heidelberg, Germany

[2]LBT Observatory, University of Arizona, Tucson, Arizona, USA

[3]Arcetri Astrophysical Observatory, Firence, Italy

[4]Max-Planck-Institut für Astronomie, Heidelberg, Germany

Correspondence
J. Heidt, Landessternwarte, Zentrum für Astronomie der Universität Heidelberg, Heidelberg, Germany.
Email: jheidt@lsw.uni-heidelberg.de

Abstract

The Seyfert 2 galaxy NGC 2273 is a prime target to explore how active nuclei can be fed. It has a star-forming innermost nuclear ring with a radius of 0.33kpc from where material may be funneled to the supermassive black hole in its center. In this article, we discuss high-resolution adaptive optics aided JHKs images of NGC 2273 taken with the Large Binocular Telescope. Using Galfit we decomposed the innermost part of NGC 2273 into a core, a disk, and a ring using 58 parameters, 44 of them were used to describe the ring. The stellar mass of the ring was found to be 12 $\times 10^8 M_\odot$, a factor of 10 higher than its molecular gas mass. A continuous gas flow via the main stellar bar of NGC 2273 during the lifetime of the bar of up to 10 $M_\odot yr^{-1}$ is required to provide the fuel for the formation of the stars unless the star formation efficiency is on the order of 10%. This does not affect the fueling of the nuclear source as the amount of molecular gas required for this low-luminosity active galaxy to achieve this is on the order of $10^4 M_\odot$ only.

KEYWORDS

galaxies: active, galaxies: individual (NGC 2273), galaxies: Seyfert, instrumentation: adaptive optics, methods: numerical

1 | INTRODUCTION

One of the long-standing questions in active galactic nuclei (AGN) research is how AGN are ignited and how their activity is maintained over several hundred million years. The various correlations between the mass of the supermassive black hole (SMBH) in the center of active and inactive galaxies and the properties of the hosting galaxy itself such as bulge velocity dispersion, mass, and luminosity (eg. Ferrarese & Merritt 2000; Gebhardt et al. 2000; Marconi & Hunt 2003; Häring & Rix 2004) leaves no doubt that they coevolve in some way. The SMBH and the host galaxy are obviously not independent entities.

Thus, the host galaxy must feed the AGN and is responsible for the SMBH growth in particular as gas must be transported to the center. There are several mechanisms

proposed which may be necessary for or at least support SMBH growth. These are major and minor mergers, cold accretion as well as secular mechanisms in the host galaxy itself such as (inner) bars and spiral arms, etc., acting as non-axisymmetric potentials.

The general view is that major mergers and/or galaxy interactions are the dominant fueling mechanism for high SMBH mass ($>10^8 M_\odot$) at high redshift, while secular evolution dominates in low-luminosity AGN in the nearby Universe (e.g., Hopkins et al. 2008; Hopkins & Quataert 2010; Kormendy et al. 2011).

One of the key questions is how the material is brought to the very center from the last few kpc's. For AGN dominated by secular evolution kiloparsec-sized bars (triggered externally or internally) are able to remove the angular momentum. Gas is then stalled near the location of the inner Lindblad resonance (ILR) from where dynamical instabilities such as nuclear spirals, dynamical friction or bars-within-bars may funnel the gas to the SMBH on pc-scales (e.g., Martini et al. 2001; Kim & Elmegreen (2017).

A comprehensive description of the various mechanisms and how they work on which timescales and spatial scales can be found in Storchi-Bergmann & Schnorr-Müller (2019).

While it is observationally relatively straightforward to study feeding on galactic scales, it becomes increasingly hard towards subgalactic scales because high-resolution observations least affected by dust are necessary. This can be done best with observations of low-luminosity, low-redshift AGN of type 2 as the impact of the bright core itself is minimized.

To fully understand how the AGN is fed multi-wavelength observations are required. High-resolution optical/NIR observations, for example, allow to study the (stellar) mass and its kinematics and hence to probe the gravitational potential. At the same time, analyzing the ionized gas and the kinematics in these sources gives clues on the interstellar medium (ISM), and may show evidence for inflow/outflows in combination with radio data. Probably most important are observations of the distribution of the molecular gas as this is thought to be the main fueling ingredient. Thanks to high-resolution facilities such as ALMA and NOEMA, molecular gas can now be studied on parsec scales.

The barred spiral galaxy NGC 2273 (=MRK 620) at a redshift of $z = 0.006138$ (de Vaucouleurs et al. 1991) is a prime target for such studies. It is a low luminosity ($L_{bol} = 10^{44.05}$ erg s^{-1}, Woo & Urry (2002)) type 2 Seyfert galaxy (Huchra et al. 1982) showing broad polarized Balmer lines (Moran et al. 2000). The mass of the SMBH in its center has been found to be $7.5 \times 10^6 M_\odot$ (Kuo et al. 2011). The source was found to be Compton thick ($N_H \geq 10^{24}$ cm^{-2}(Awaki et al. 2009)). NGC 2273 has an angular size of $3.6' \times 2.4'$ on POSS plates (Nilson 1973) seen at an inclination of 41°. It has an inner and two outer pseudo-rings, formed by separate sets of spiral arms (e.g., van Driel & Buta 1991), extending over the whole galaxy. The innermost region with a diameter of $8''$ (roughly 1 kpc) around the bulge was first classified as a secondary bar based on ellipse fits by Mulchaey et al. (1997). This was corrected a few years later using high-resolution narrow-band imaging of the Hubble Space Telescope (HST) with the Wide Field and Planetary Camera 2 (WFPC2) by Ferruit et al. (2000) and by Erwin (2004). They revealed that the innermost region actually displays a *fourth*, bright, star-forming nuclear ring connected to the center via two luminous blue nuclear spiral arms (Erwin & Sparke 2003). We refer to this region as the "central structure/region" of NGC 2273. It is visible, for example, in Malkan et al. (1998), Ferruit et al. (2000), Martini et al. (2003a).

A number of observations complementary to the morphological studies mentioned above by e.g., Barbosa et al. (2006), Barbosa et al. (2009), Mundell et al. (2009), Domínguez-Fernández et al. (2020), and Ma et al. (2021) have resulted in a fairly coherent picture of the center of NGC 2273.

Barbosa et al. (2006) derived from the stellar kinematics of the inner $5''$ that the radial velocity field is dominated by rotation. They found a decrease of the velocity dispersion at about 200–300 pc from the center cospatial with the ringlike structure derived from morphological studies and concluded that this ring-like structure traces recently formed stars that partially keep the cold kinematics of the gas out of which they have formed. Using the same data set Barbosa et al. (2009) analyzed the kinematics of the ionized gas in the narrow line region of NGC 2273 and found 4 distinct kinematic gas components. Two of them are coincident with two radio components also detected by Mundell et al. (2009) and which can be interpreted as evidence for the interaction of a small radio jet with the circumnuclear ISM due to outflows. The other two seem to be coincident with the nuclear spiral arms detected by Erwin & Sparke (2003). Barbosa et al. (2009) derived a mass outflow rate which is a factor of ∼30 larger than the accretion rate for NGC 2273 and concluded that the outflows do not originate from the nucleus but are rather due to gas from the circumnuclear ISM being pushed away by a nuclear jet or wind. Ma et al. (2021) came to a similar conclusion from their Baldwin–Phillips–Terlevich (BPT) mapping using narrow-band images. They derived two low-ionization nuclear-emission (LINER) types in NGC 2273, one of which was very close to the center indicative of jet-ISM interaction, the other one associated with the ring structure indicative of photoionization by an absorbed (filtered) AGN or starburst in the ring.

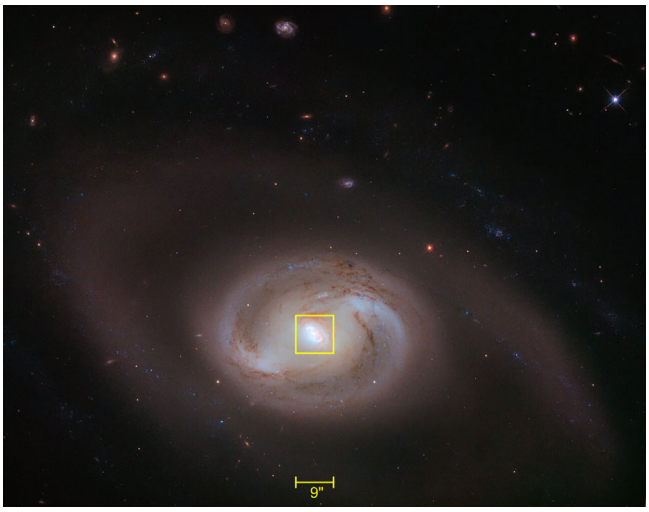

FIGURE 1 Hubble Space Telescope WFC3 multicolor-image of NGC 2273 to highlight its various spiral arms, bars, and rings. Observations through five filters (FF336W (U), F438W (B), F184W (I), F160W (H), and F673N (SII)) have been used to create this image. FOV is $2.59' \times 2.01'$, north is 6.8° left of vertical. The innermost bluish ring a few arcsec in diameter is the target of the present study. The region analyzed in this paper is indicated. Image credit: ESA/Hubble & NASA, J. Greene.

Domínguez-Fernández et al. (2020), finally, investigated the properties of the molecular gas in the center of NGC 2273 and found (a) that the gas follows the same kinematics as stellar and neutral gas components and is rotating in the galaxy disk, (b) no evidence for inflows/outflows, and (c) higher gas concentrations coincident with the inner dusty spiral arms detected by Erwin & Sparke (2003). They also derived the mass of the molecular gas in the circumnuclear region roughly tracing the innermost ring to 1.26 $\times 10^8 M_\odot$. In sum, NGC 2273 has a main bar and a nuclear ring suspected to coincide with the ILR of the main bar where gas accumulates, where stars are formed and from where the gas seems to be funneled to the AGN via two inner spiral arms. In Figure 1 we show an HST image of NGC 2273 showing its complex morphology.

Apart from an analysis of the stellar kinematics in the center of NGC 2273 by Barbosa et al. (2006) and the common agreement that the ring is star-forming, the stellar content in the inner part of NGC 2273 has not been addressed yet. This is particularly interesting for the nuclear ring, as a comparison of its stellar content and gas mass allows to estimate the star formation efficiency in the presence of an active nucleus.

In this paper, we present and discuss adaptive optics-assisted high-resolution JHKs images of NGC 2273's central region using the Large Binocular Telescope (LBT) and the LBT Utility Camera in the Infrared (LUCI). We tried to decompose the images into various components consisting of a bulge, a disk, a ring, and inner spirals using a fully 2-dimensional modeling algorithm provided by Galfit (Peng et al. 2010) for the first time. Due to the very complex structure of the innermost part of NGC 2773, we succeeded in fitting a bulge, a disk, and a ring using 58 free parameters in total only. 44 of these parameters are used to describe the complex nuclear ring. Our models go beyond ordinary elliptical profiles using azimuthal shape functions. We also created a more simple, axis-symmetric model to analyze the structure of the ring.

The paper is organized as follows. In Section 2, we describe our observations, the instrumentation, and the data reduction. In Section 3, we give an introduction to Galfit and our fitting procedure because our fits with 58 free parameters are more complex than the fits usually done with Galfit. This is followed by the presentation of our results which includes derivation of the properties of the innermost ring of NGC 2273 from our best-fit parameters. In Section 4, we discuss our models and how they can be improved. Finally, we examine the stellar content of the ring in detail and how it fits to its global properties.

We assume a flat ΛCDM cosmology with $H_0 = 70$ km s^{-1} Mpc^{-1} and $\Omega_m = 0.3$ throughout. Using this cosmology, the angular scale is 0.126 kpc per arcsecond at $z = 0.0061$.

2 | OBSERVATIONS AND DATA REDUCTION

The data of NGC 2273 were acquired with the LUCI1 instrument at the LBT (Seifert et al. 2003) supported through FLAO (first light adaptive optics, Esposito et al. (2012)) during a commissioning run on March 21, 2016. The data were recorded in the JHKs bands with the N30 camera offering a FoV of $30'' \times 30''$ having a scale of 0.015″/pixel. The observing conditions were very good with ambient seeing mostly around 0.7″.

The LBT's FLAO system includes a pyramid-based wavefront sensor analyzing the atmospheric turbulence with a grid of 30×30 subapertures. 672 actuators control the adaptive secondary mirror and correct the distortion caused by seeing with a frequency of up to 1 kHz. The reference object for the FLAO system was the nucleus of NGC 2273 itself as a (successful) test of whether a point source with diffuse extended emission may be suitable as a reference object. This observing mode is now frequently used at the LBT.

Ten exposures of NGC 2273 were taken in the J and H band and 9 exposures were acquired in the Ks band. The integration time per image was 60s in all cases. The telescope was slightly offset between each of the images to allow for the correction of bad pixels. In addition, six

frames with the same integration times were taken in all three filters far off the object for sky subtraction purposes. They were required because the area covered by NGC 2273 is larger than the area provided by the N30 camera. Finally, two images of the standard star S9142 listed in Persson et al. (1998) were recorded in each filter to set the zero point.

The reduction of the data was carried out with the image reduction and analysis facility IRAF (Tody 1986). We first corrected all images for non-linearity and for bad pixels. Next, the spatial sky variations were subtracted from the science frames using a scaled master sky frame whose median was set to zero. As no significant change in the gradient was present between the individual sky frames, all six sky frames were used to create a master sky frame in each band by subtracting their median and then median-combining them. We took the median of the southern region of the science frames as the sky level which we subtracted as absolute sky level. This was justified in spite of the fact that the size of the galaxy is larger than the area covered by LUCI for the following reasons: the average sky level in the southern region on the 6 sky frames was 167.2 ± 5.5, 1153.3 ± 57.0, and 602 ± 11.6 ADU for J, H, and Ks, respectively. This was (by curiosity) in all three filters higher than what we measured in the same southern regions of the frames targeting NGC 2273 (155.8 ± 10.4, 1148.3 ± 19.0 and 588.7 ± 14.9 ADU in J, H, and Ks). In addition, we had J and H sky values which were lower than measured on the object frames. On top of that, the "sky" variations were >20% in all three filters. This led us to conclude that the contribution of the galaxy in the southern region on the frames is negligible in all cases and the sky by far dominates.

Finally, each science frame was divided by a master flatfield. This masterflat was constructed from a set of flats using LUCI's calibration unit with a halogen lamp on and the halogen lamp off. The lamp on/off frames were pairwise subtracted to remove static features, normalized, and median-combined. In the end, the images in each filter were stacked by averaging and rejecting the pixel with the lowest and highest intensity at each position. The images were aligned with respect to the pixel with a maximum value of NGC 2273 before stacking.

The flux calibration was achieved by using the images of S9142. To tie the photometry of the science frames and the photometric standard star frames together, the images were corrected for atmospheric extinction using data provided by the observatory and for galactic reddening following Schlafly & Finkbeiner (2011).

Because of the absence of stars on the science frames, we can not measure the Strehl ratio on our final images. However, given that the FLAO system has "seen" NGC 2273 as a reference object with 15th magnitude and since the ambient observing conditions were very good (0.7″ seeing), we would expect a Strehl ratio of ∼ 10-30% (see Esposito et al. (2012)). A comparison to HST data from NGC 2273 in the same passband allows a qualitative estimate. In Figure 2 we compare our H-band image of NGC 2273 with H-band images taken with the WFC3/IR (proposal-id 12185, Greene, 0.13″/pixel) and NICMOS/NIC2 (proposal-id 7172, Rieke, 0.075″/pixel) after rebinning them to the same spatial sampling as on our images (0.015″/pixel). Clearly, the NICMOS image appears sharpest since it is diffraction-limited and well sampled, while the WFC3 image suffers from undersampling. Overall, the LBT-AO image traces the structure

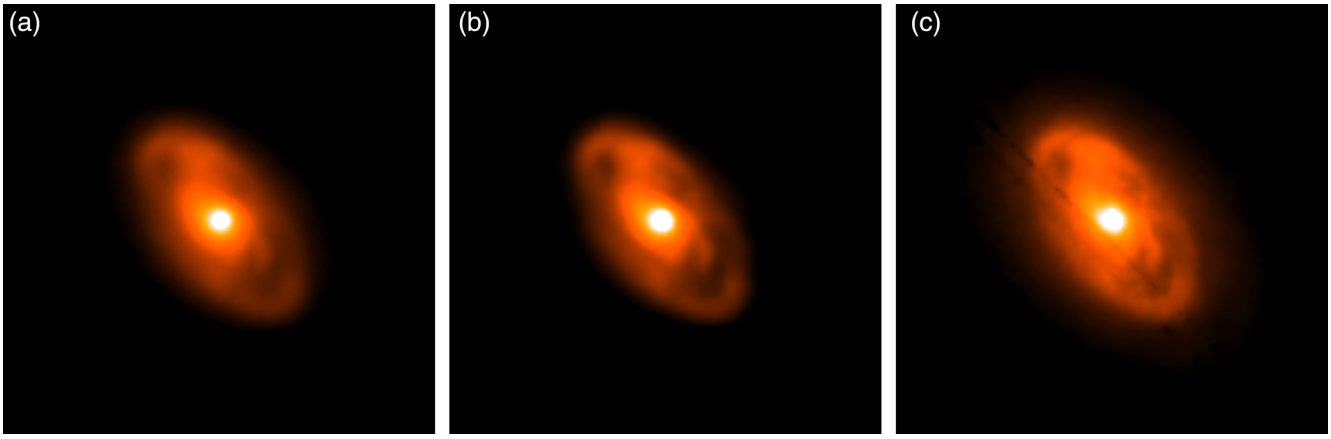

FIGURE 2 H-band image of NGC 2273 with LUCI1/FLAO at the LBT (left), and with WFC3/IR at the HST (center) and NICMOS/NIC2 at the HST (right). The HST images have been rebinned to the same spatial sampling as the LBT image for direct comparison. FOV is 9″ × 9″ in all cases. A linear scale was used to produce the images. The diagonal dark stripes on the NICMOS image are detector artifacts. While the NICMOS images are the sharpest with some fine details (which could well be due to patchy dust in the center of NGC 2273), the LBT image accurately traces all structures seen in the HST images.

seen in the HST images pretty well even if it is not fully diffraction-limited. Unfortunately, we can not use the HST images to empirically estimate the image quality (Strehl) on our image as the core of NGC 2273 is well resolved on all three images. We measure 0.4–0.5″ FWHM with a slight elongation in east-west direction (also found by Ferruit et al. (2000) and Ma et al. (2021)). This is a factor of 3–4 wider than the diffraction limit on the HST and a factor of about 10 wider than the diffraction limit for the LBT.

3 | ANALYSIS AND RESULTS

The central region of NGC 2273 in the JHKs bands is shown in Figure 3a–c. A complex structure becomes apparent consisting of a disk and a ring connected by inner spirals to the center. The ring is not closed on the eastern and western sides. The structure is similar to the one derived by Erwin & Sparke (2003). To extract their physical properties, we modeled these structures using Galfit.

3.1 | Our application of Galfit

We will now give a brief overview of Galfit and the functionalities we used. This is necessary in order to understand our resulting best-fit models, which are described by a large set of components and parameters. More details can be found in the Galfit user's manual.

The radial profile used for our fits is the Sérsic profile described by

$$\Sigma(r) = \Sigma_e \exp\left[-\kappa\left(\left(\frac{r}{r_e}\right)^{\frac{1}{n}} - 1\right)\right], \quad (1)$$

in which $\Sigma(r)$ is the surface brightness at radius r, Σ_e the surface brightness at the effective radius r_e, and n the concentration parameter. The effective radius r_e is defined as the radius that contains half of the total luminosity. To ensure this definition, κ is not a free parameter. If the boxyness parameter mentioned in the user's manual is set to zero, as it is for our fits, the radial coordinate of the radial profile functions is given by

$$r(x,y) = \left((x-x_c)^2 + \left(\frac{y-y_c}{q}\right)^2\right)^{\frac{1}{2}}. \quad (2)$$

That allows the profile function to have an elliptical shape for the axis ratio $q < 1$ around the center (x_c, y_c). Furthermore, the radial profiles can be rotated with a position angle of θ_{PA}. Our disk and bulge components are solely described by a Sérsic profile. The main mathematical difference is visible in the concentration parameter n (a generally higher value for the disk component) and even more prominently in the effective radius r_e as the bulge is a much more compact object.

A ring can be seen as a radial luminosity profile from which an inner and outer part are cut-out. This is the idea behind Galfit's truncation functions in which a radial profile is multiplied with an asymptotic function with values between zero and one, truncating the radial profile at a given radius in a continuous way. The asymptotic function $f(r)$ used is a modification of the hyperbolic tangent function for an inner truncation and $(1-f(r))$ for an outer truncation. Next to the parameter r_{break}, which corresponds to the radius at which the asymptotic function has the value of 0.99, the other necessary parameter is Δr_{soft} giving the length of the asymptotic function between $f(r) = 0.01$ and $f(r) = 0.99$. Furthermore, there are four optional parameters to change the center, axis ratio, and position angle of the truncation function if these parameters from the connected radial profile do not fit the truncation. Both parameters r_{break} and Δr_{soft} correspond to the pixel-radius on the semi-major axis as the truncation function can also have an elliptical shape. The normalization parameter for truncated profiles is Σ_{break}, the surface brightness at r_{break}, while the total apparent magnitude is used for the untruncated profiles instead.

Not every object that we observe in the sky is perfectly elliptical. In our case, NGC 2273 has a ring that is barely closed on the eastern and western sides. It is also connected to the inner spiral which leads to locally thicker parts of the ring. For such cases, Galfit includes a category named azimuthal shape functions to describe these structures differing from the optimal elliptical shape. They can be divided into two subcategories which are both used for our ring fits. The Fourier modes build the first one and modify the radial coordinate according to

$$r_{mod}(x,y) = r(x,y)\left(1 + \sum_{m=1}^{\infty} a_m \cos(m(\theta + \phi_m))\right). \quad (3)$$

In Equation (3) m is the number of the Fourier mode, a_m its amplitude, ϕ the phase angle, and θ the polar angle for the original radius $r(x,y)$ from Equation (2). The second subcategory is given by the bending modes

$$y' = y + \sum_{m=1}^{\infty} a_m \left(\frac{x}{r_e}\right)^m \quad (4)$$

which represents a transformation $(x,y) \mapsto (x,y')$. Here m and a_m are the number and amplitude of the bending modes. It is hard to imagine solely from Equations (3)

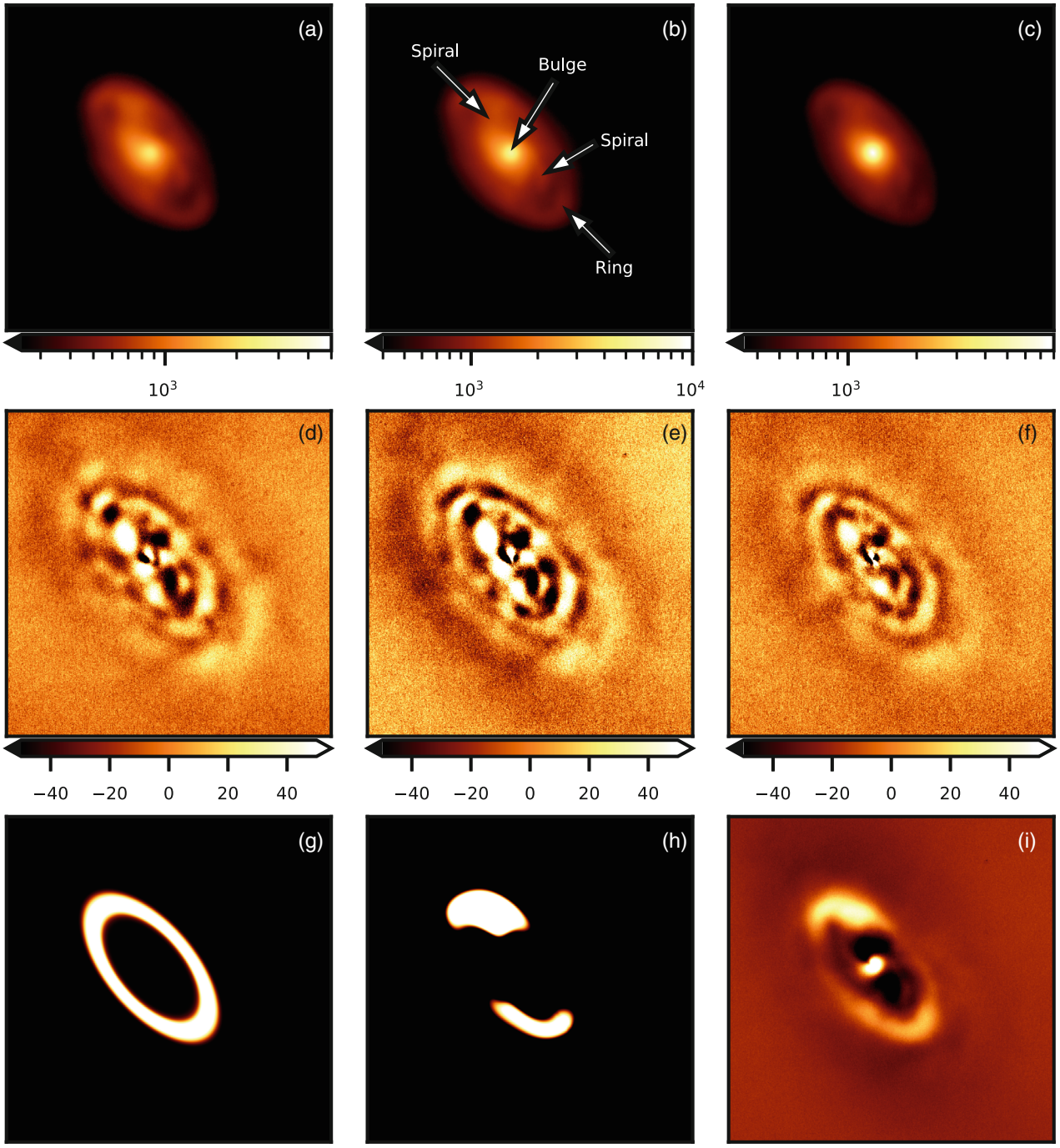

FIGURE 3 (a–c) Cutouts of the central region of NGC 2273 in the J-band (left panel), H-band (middle panel), and Ks-band (right panel). The components that we fitted (or tried to fit) and which we discuss in the text are labeled in the H-band image. (d–f) The residuals after subtraction of the 3-component fit consisting of a bulge, disk, and ring in JHKs ordered like (a–c). (g,h) The simple-ring model and the complex-ring model in the H band. (i) The residual image after subtraction of a one-component disk-fit in the H-band. In each image, the FoV is $9'' \times 9''$. North is up, east is left. Intensities are given in ADU.

and (4) what the distortion of a radial profile by a set of azimuthal shape functions looks like. A visualization for a few selected modes is given in Peng et al. (2010). The difference between the complex-ring model with azimuthal shape functions and the simple-ring model without them in our case is presented in Figure 3g,h.

3.2 | Component fitting

An input-file for Galfit contains not only the models and initial parameters but also image and control parameters. We reduced the image size to the area of $9'' \times 9''$ to extract the central structure and to minimize the

duration of the fitting process. The input-images can be seen in Figure 3a–c. We specified the point spread function (PSF) given by the LBT for the JHKs filters with a convolution box over the whole image to improve the quality of the fits. As we could not determine the PSF from the images directly, a theoretical PSF composed of a diffraction-limited core with a Strehl ratio of 20% and a seeing-halo was adopted. For the seeing halo, we used a Gaussian profile with $0.7''$ FWHM. We set the number of coadded images in the header of the input-images to one because then Galfit calculates a σ-image of the input-data $f(x, y)$ according to

$$\sigma(x, y) = \sqrt{\frac{f(x, y) - \langle \mathrm{sky} \rangle}{\mathrm{Gain}} + \sigma^2_{\mathrm{sky}}}, \tag{5}$$

in which $\langle \mathrm{sky} \rangle$ is the mean of the sky approximated by Galfit and σ_{sky} its standard deviation. The Gain-value is taken from the header of the input-image. As the sky has already been subtracted, we set $\langle \mathrm{sky} \rangle = 0$ manually to prevent Galfit from calculating a wrong value based on the bright structures in the central region. The value σ_{sky} is approximated in each filter as the square-root of the mean of the determined sky-levels since the latter are Poisson-distributed and differ below 2% relatively from the mean. As discussed in section 2 the contribution by the galaxy was found to be negligible in the southern regions of the frames and suffered from sky variations on the order of 20%. We thus determined σ_{sky} directly on the science frames. Further we correct Galfit's χ^2_ν-value

$$\chi^2_{\nu,\mathrm{cor}} = \sqrt{N}\chi^2_\nu, \tag{6}$$

because the number of coadded images N has not been included to the calculation of $\sigma(x, y)$ yet.

One could start fitting all components together but this is often not the most efficient procedure, especially not for a large number of free parameters. The result will most likely be good in a mathematical sense but not physically realistic because the algorithm may just find a local minimum in the χ^2_ν-surface far off the most realistic minimum. This means that if the starting parameters are too far away from a physically realistic model, then the result of the fit will also probably not be realistic. The strategy we used was first to simply fit three different components one after another: a disk, a bulge representing the very center, and a ring. Starting with the disk, we guessed the starting parameters from the input-image and optimized them in a one-component disk-fit. Traditionally, the very center (AGN) is taken to be a point source and is represented by the PSF itself. However, it turned out that this was not the best approach in our case. NGC 2273 is a Seyfert 2 galaxy, where one would not expect the core to be too prominent. Indeed, we do not detect a prominent core in spite of the potentially high Strehl ratio. The core is more complex because it is elongated in E-W direction and because of the presence of the inner spirals, which seem to dominate the flux. We thus decided to fit a small bulge as a means to get rid of most of the flux from the core leaving as much as possible realistic parameters for the other two components. Next, we fitted both components together and optimized the starting parameters for the ring fit (radial profile + inner and outer truncation) on the residuum of the two-component fit. Further, we added different Fourier and bending modes to the ring to get closer to the real shape. They were also added one after another and optimized on the two-component disc/bulge-fit. In the very end, all components and azimuthal shape functions were fitted together in a three-component fit with the resulting parameters from the individual steps as our starting parameters. The advantage of this technique is that we could see when parameters for a component became unrealistic, which parameter was the reason for that, and thus, which starting parameter we had to change.

The final three-component fit had 58 free parameters. 44 of the 58 parameters are used to describe the complex ring. Even though this is the best fitting model we could develop to describe the ring's luminosity distribution, the large amount of Fourier and bending modes deform the Sérsic profile in such a way that the structural parameters of the radial profile are no fitting parameters on their own. Some of the Fourier modes, for example, modify the ellipticity and/or thickness of the ring (see e.g., Peng et al. (2010), their fig. 9). This leads to a degeneracy between some of the azimuthal shape function parameters and the regular ones. To find more suitable values, we thus fitted a closed ring without Fourier and bending modes on the residuum of the two-component disk-bulge fit. The difference between the complex-ring model and the simple-ring model is visualized in Figure 3g,h.

3.3 | Fit results

Figure 3d–f shows the images after subtraction of our three-component fit consisting of a bulge, disk, and an open ring. The residuals amount to about 2% of the total flux, which means that 98% of the light was included in the three components. Because of the probably patchy dust distribution in the very center, the residuals look irregular. They become less strong towards longer wavelengths as the effects caused by dust are less prominent. Irrespective of that it is hardly possible to distinguish real features from apparent ones due to imperfect modeling. Also because of this, the inner spiral arms of NGC 2273 are not clearly visible. To highlight the spiral structure more clearly, we show

TABLE 1 General results for the fits with three components in all three bands.

Filter	Component	– Sérsic –	mag	r_e [pixel]	n	q	θ_{PA} [°]
		Truncation	Inner or outer	r_{break} [pixel]	Δr_{soft} [pixel]	q	θ_{PA} [°]
J	Ring	-Sérsic-	13.53	115.84	0.050	0.50	40.04
			…	(0.67)	(0.001)	(0.01)	(0.05)
		Truncation	Inner	141.64	40.93	0.50*	40.04*
			…	(0.57)	(1.09)	(0.01*)	(0.05*)
		Truncation	Outer	175.55	0.76	0.50*	40.04*
			…	(1.76)	(3.00)	(0.01*)	(0.05*)
J	Disk	-Sérsic-	11.31	163.61	1.47	0.72	52.35
			(0.01)	(0.06)	(0.01)	(0.01)	(0.02)
J	Bulge	-Sérsic-	16.98	12.52	0.44	0.74	2.45
			(0.01)	(0.05)	(0.01)	(0.01)	(0.66)
H	Ring	-Sérsic-	12.79	113.09	0.054	0.50	41.17
			…	(0.40)	(0.001)	(0.01)	(0.05)
		Truncation	Inner	141.79	44.07	0.50*	41.17*
			…	(0.55)	(1.04)	(0.01*)	(0.05*)
		Truncation	Outer	172.93	2.81	0.50*	41.17*
			…	(0.57)	(1.71)	(0.01*)	(0.05*)
H	Disk	-Sérsic-	10.22	197.89	1.79	0.72	49.73
			(0.01)	(0.07)	(0.01)	(0.01)	(0.02)
H	Bulge	-Sérsic-	15.26	13.89	0.76	0.80	-27.23
			(0.01)	(0.03)	(0.01)	(0.01)	(0.29)
Ks	Ring	-Sérsic-	12.38	112.14	0.055	0.51	43.02
			…	(0.31)	(0.001)	(0.01)	(0.06)
		Truncation	Inner	139.80	40.36	0.51*	43.02*
			…	(0.55)	(1.06)	(0.01*)	(0.06*)
		Truncation	Outer	173.17	2.59	0.51*	43.02*
			…	(3.36)	(5.80)	(0.01*)	(0.06*)
Ks	Disk	-Sérsic-	10.09	157.33	1.61	0.71	49.58
			(0.01)	(0.04)	(0.01)	(0.01)	(0.02)
Ks	Bulge	-Sérsic-	13.22	15.97	1.04	0.89	-18.59
			(0.01)	(0.02)	(0.01)	(0.01)	(0.18)

Note: For the Sérsic profiles derived for the disk, bulge and the ring, we list the magnitude, half-light radius r_e in pixels, the Sérsic index n, the ellipticity q and the position angle Θ_{PA}. For the ring, we show the results for the model with a closed ring, and give the inner and outer truncation break radius r_{break} as well as the length of the asymptotic function Δr_{soft} in addition. We give the luminosities for the model with the open ring as these are the ones we used to derive physical quantities of it. The full set of parameters for the model with the open ring can be found in the Tables A1–A3 in the Appendix. To make the tables as well readable as possible, we list the statistical uncertainties for each parameter based on the covariance matrix of the fit individually in brackets below. See Section 3.1 for details.

*Adopted from the basic Sérsic profile.

the residual image after subtraction of the one-component disk-fit in the H-band in Figure 3i. Now, the complex structure of the ring and a faint spiral arm on the eastern and fragments of the other one on the western side winding clockwise around the "black spots" can clearly be seen. The latter is most likely covered by dust, at least partially.

In Table 1 we show the results for the disk and bulge from our three-component fit and the structural

parameters for the closed ring. For the latter, we give the integrated brightness derived for the open ring. The entire set of 58 fit parameters including the open ring can be found in the Appendix in Tables A1–A3. As the normalization parameter for the truncated Sérsic profile used for the open ring is the surface brightness at the break radius instead of the apparent magnitude, the latter was calculated by integrating the counts across the entire model.

3.3.1 | Properties of the disk

We derived for the disk of NGC 2273 JHKs magnitudes of 11.31, 10.22, and 10.09, respectively. This results in J−H and J−K colors of 1.09 and 1.22. The disk of NGC 2273 seems to be 0.4–0.5 mag redder than what has been inferred for a sample of nearby, bright spiral galaxies by Möllenhoff & Heidt (2001). They found J−H and J−K colors of 0.75 ± 0.27 and 0.71 ± 0.25. This is not surprising given that Möllenhoff & Heidt (2001) fitted across the whole galaxy, while we fitted only the central 9″ (although the brightness of the disks was derived by integration from the center to infinity). The total apparent magnitude of NGC 2273 in the H-band is 8.771 ± 0.016 mag (Skrutskie et al. 2003), which means that our model for the disk in the H-band accounts for 26% of the total flux. The position angle of the disk is within 51° ± 3% in each filter. A similar position angle for the disk has been derived by Erwin & Sparke (2003).

Two factors that impact the inferred parameters of the disks are the presence of the remaining spiral structure and the determination and subtraction of the sky level. The former may also affect the other two components, given the spiral's connection to the outer ring and central bulge, but the disk is the sole component that extends throughout the entirety of the spiral. To minimize the χ^2_ν-value, it is preferable to account for any structure present, and hence the disk fit must incorporate a portion of the spiral. With the disk's elliptical symmetry, the fit leaves behind two over-fit voids visible north and south of the center in Figure 3i. The second factor affecting the disk's parameters is the subtraction of the sky level, which we determined as the median of the southern region in the uncut $30'' \times 30''$ images. Since our images only cover a portion of NGC 2273, a fraction of the determined sky level arises from the disk, assuming it extends throughout the galaxy. Our best-fit model in the H-band predicts a value of the disk in this region below 2% of the subtracted sky-level. This corresponds to 8% of the average disk brightness in the cutout $9'' \times 9''$ images. Concerning the disk's best-fit magnitude, the two factors are competing against each other and it is unclear whether the real disk's magnitude, if at all, is higher or lower. However, it is certain that both factors lead to a lower concentration parameter n, as they elevate the prominence of the core relative to the outer region of the Sérsic profile.

3.3.2 | Properties of the ring

For the fit to the ring using a model with an open ring, we derive JHKs magnitudes of 13.53, 12.79, and 12.38, respectively. The resulting J−H and J−K colors are 0.74 and 1.15mag. The J−H color is about 0.35mag bluer than what we found for the disk while the J−K colors are similar. Naively, one would expect the NIR colors of star-forming regions to be very blue. But that is true in the optical only. For example, based on a study of the centers of 5800 galaxies from the SDSS, Eminian et al. (2008) have shown that galaxies with higher specific star formation rates have redder near-IR colors. This could be due to thermally pulsing asymptotic giant branch stars, which dominate the H- and K-band light of a galaxy following a burst of star formation. We found very little scatter in the position angles of the ring as function of wavelength. They are all around 41°, which is offset by about 10° from the position angle for the disk. The break radii $r_{\rm break}$ for the inner and outer truncation are constant within 2% over all filters. If we use their averages, i.e. $r_{\rm break} \approx 141$ pixel for the inner and $r_{\rm break} \approx 174$ pixel for the outer radius, the thickness can be approximated to 33 pixels on the semi-mayor axis. This corresponds to a ring with a radius of $r \approx 2.6''$ (0.33 kpc) and a thickness of $t \approx 0.5''$ (0.06 kpc) on the semi-major axis. The axis ratio $q \approx 0.5$ is almost constant over each filter leading directly to the radius and thickness on the semi-minor axis. However, as Figure 3i reveals, the ring structure is more complex in reality and the model here is rather simplified. The numbers for the diameter, position angle, and ellipticity match well the ones derived by Erwin & Sparke (2003).

4 | DISCUSSION

4.1 | Technical aspects

Based on AO-supported images of NGC 2273 taken with the LBT in the JHKs bands, we developed models describing the two-dimensional luminosity profile of three components in the central region: a bulge representing the core, a disk, and a ring. The χ^2_ν-values are $\chi^2_{\nu,\rm cor} = 1.632$, $\chi^2_{\nu,\rm cor} = 1.508$ and $\chi^2_{\nu,\rm cor} = 1.275$ in the JHKs bands, respectively. This indicates formally a good fit. Our models seem to fit better for longer wavelengths which is not unexpected as the central part of NGC 2273 has a substantial amount of patchy dust, which is more prominent in the bluer bands.

Our fits do not include a model for the inner spirals since we can hardly distinguish the spirals from the residuals of the other components for the best-fit (see Figure 3d–f). This is mainly due to the bright ring whose residua coincide with the onset of the inner spiral structure. We tried to add the last component but failed. Obviously, adding a few more parameters to describe the inner spirals on top of 58 parameters already used to describe the core, the disk, and the ring lead easily to highly degenerate results.

Formally, it should be possible, to trace the inner spiral arms from the ring down to the center which is from about 330pc (2.6″) radius. The torus of AGN is typically a few pc in diameter (Elitzur 2006), which sets the inner limit. With a pixel scale of LUCI of 0.015″/pixel equivalent to 2pc at the distance of NGC 2273 and a diffraction limit of 0.066″ of the LBT in the K-band equivalent to 8pc we should in principle be able to trace the inner spiral arms well enough. Given the observing conditions and a stably working AO during the night, the image quality was as expected (also during observations of other sources before/after NGC 2273). The fits may have been somewhat better, if we could have used an observed PSF for the deconvolution. This is not possible, however. The AO correction is different if a point source plus underlying nebulosity is used as reference source compared to the correction using a pure point source as reference source.

Thus, to do it better, one should reduce the extinction by going to longer wavelengths. This would lead to more accurate modeling at the expense of a less good diffraction limit and a much higher sky background if on ground. For example, the interferometer at the LBT offers the spatial resolution of a 22.8m telescope. For the M-band at 4.5μm, the diffraction limit is similar to the K-band with LUCI but the sky is about 6mag brighter. A viable alternative would be to go to space and to use JWST's IFU unit at NIRSPec to map the nuclear structure (and the ring) of NGC 2273. The diffraction limit would be about 25% larger but the impact by the (near)infrared background minimized. On top of this, a stable PSF would ease modeling.

4.2 | The ring

The most important result of this study is that the nuclear ring with about 2″ in diameter has been fully 2-dimensional modeled in NGC 2273 for the first time. With JHKs magnitudes of 13.53, 12.79, and 12.38mag (6.17, 7.84, and 7.45 mJy) the ring is fairly bright in the NIR. To have an estimate of the stellar mass of the ring we will use the mass to light ratio relation in the NIR for an "old" stellar population derived by Thronson et al. (1988) to

$$M_{\star,\mathrm{old}}(\mathrm{M}_\odot) = C_{\mathrm{JHKs}} \times \mathrm{D}^2(Mpc) \times \mathrm{F}_{\mathrm{JHKs}}(Jy) \qquad (7)$$

with the constant C = $2.3 \times 10^8, 2.1 \times 10^8$ and 2.6×10^8 for J, H, and Ks, respectively. Using our fluxes and the mean distance D = 28.9 Mpc of NGC 2273 from Theureau et al. (2007) we derive $\sim 12 \times 10^8 \mathrm{M}_\odot$ (11.9, 7.0 and 16.2 $\times 10^8 \mathrm{M}_\odot$ for JHKs) for the stellar mass in the ring. The dynamical mass of NGC 2273 within the inner 12 kpc has been determined to be $1.4 \times 10^{11} \mathrm{M}_\odot$ based on HI measurements by van Driel & Buta (1991). Thus a substantial fraction of the stellar mass in NGC 2273 could well be in the ring. The derived stellar surface mass density of the ring would be $\Sigma_\star \sim 10^4 \mathrm{M}_\odot/\mathrm{pc}^{-2}$. This is a factor of 10 below the maximum surface mass density of $\Sigma_\star^{Max} = 10^5 \mathrm{M}_\odot/\mathrm{pc}^{-2}$ derived for stellar systems by Hopkins et al. (2010).

It is clear that the stellar mass and stellar surface mass densities calculated above are highly uncertain. The relation used to convert luminosities into masses was derived for an "old" population of stars for disk regions in the Milky Way, while we here discuss the properties of a presumably star-forming ring. This may lead to a lower conversion factor. In addition, we suffer from an unknown amount of local extinction which may lead to a higher stellar mass. Similarly, we used the fluxes derived for the model with the open ring. If the ring was closed (not detected because of extinction), the resulting mass could be higher too. On the other hand, we used NIR images where the old stellar population dominates the light after subtraction of the contribution by the disk and the core. Thus our assumptions are not too unrealistic. In the end, even if our estimates are wrong by a factor of 10, between 0.1% and 1% of the total mass of NGC 2273 could be in stellar form in the ring.

Due to the complexity involved in the modeling, morphological studies of the properties of nuclear (starburst) rings are rare. One exception is the morphological analysis of the starburst ring of 17 non-active galaxies by Ma et al. (2017); Ma et al. (2018) using HST and Spitzer data by employing a similar method (fitting the ring via truncation but without azimuthal shape functions in Galfit) as presented here. The derived median mass for the rings is $\sim 9.3 \times 10^8 \mathrm{M}_\odot$ from optical images, which is similar to what we found for our NIR-images of NGC 2273.

In a spectrophotometric analysis of the inner 2″ × 2″ of NGC 2273, Gu et al. (2003) found clear evidence of recent star-forming activity. Using stellar synthesis modeling they found that an intermediate age ($\sim 10^8$yr) and an older ($>10^9$yr) population dominate the emission with 33.4% and 56.6%, respectively. Even if this region probed is smaller than the radius of the ring, a substantial fraction of

the emission from the ring could have been spilled into the 2″ wide slit used by Gu et al. (2003) depending on the seeing. If we assume that the stars in the central region have been formed from the same gas as the stars in the ring, we could estimate the age of the ring to be $\sim 10^8 - 10^9$yr. This is practically the same age ($\sim 10^{8.5}$yr) as derived by Ma et al. (2018) for their sample of non-active galaxies with nuclear rings. This fits nicely in the idea discussed by Gu et al. (2003) that tidal interaction with NGC 2273B about 10^9yr ago may have triggered the star-formation (and also the AGN-activity) in NGC 2273.

Domínguez-Fernández et al. (2020) estimated the mass of the molecular gas in the circumnuclear region which roughly traces the innermost ring to be $1.26 \times 10^8 M_\odot$. This is about a factor of 10 less than we found for the stellar mass in the ring. If we assume that the stellar mass in the ring has been formed throughout the lifetime of the ring of 10^9 yr, we end up with a contiguous star formation rate of $\approx 1.2 M_\odot yr^{-1}$. The star formation efficiency in giant molecular clouds in which the stars in the ring presumably form is typically 1% albeit with a large scatter of 0.5dex (Grudić et al. 2019). This would require molecular gas on the order of $10^{10-11} M_\odot$ to be channeled via the stellar bar. This is quite a lot. Stellar bars have lifetimes of 1–2 Gyrs (e.g., Bournaud et al. 2005). Channeling rates of up to $10\ M_\odot yr^{-1}$ would be required to supply the amount of gas required unless the star formation efficiency is on the order of 10% for most of the time.

It is important to emphasize that the large amount of molecular gas required does not affect fueling of the AGN. Barbosa et al. (2009) estimated the accretion rate to fuel the supermassive black hole of NGC 2273 to be about $9 \times 10^{-5} M_\odot yr^{-1}$. Assuming an activity period for NGC 2273 of about 100 Myr just $10^4 M_\odot$ are required to achieve this. Given the low luminosity of the AGN it is no surprise that very little to no evidence for outflows and hence feedback in NGC 2273 has been found by Barbosa et al. (2009) and Ma et al. (2021). The SMBH itself must have been formed earlier during a phase of much higher accretion. Using the accretion rate from Barbosa et al. (2009) the time to grow to $7.5 \times 10^6 M_\odot$ is well in excess of a Hubble time.

Nuclear rings are not a unique, nor a frequent feature in Seyfert 2 galaxies. Malkan et al. (1998), found that only about 10% of 114 Seyfert 2 galaxies imaged with the HST host a nuclear ring. Most of them (but not all) have a large-scale bar. Similar numbers were derived by Martini et al. (2003a). This led Martini et al. (2003b) to conclude that the "pilepup" of bar-driven inflow into a ring is a rare occurrence.

Our purely morphological study presented here can be seen complementary to IFU studies in the NIR of other nearby AGN as carried out for example, by Busch et al. (2017), Fazeli et al. (2020b) and Fazeli et al. (2020a). These studies allow to derive a detailed view of the nuclear rings of nearby AGN such as the kinematics of their gas and stars. Unfortunately, they do not use their data to estimate the amount of stellar mass in the rings. On the other hand, as shown by Ma et al. (2018), multi-band images including Hα-data allow fairly well to get a handle on the extinction, mass and star formation rates. The HST archive contains a wealth of imaging data for NGC 2273 (see references in the introduction). Stellar masses for a sample of local Seyfert 2 galaxies could be achieved using archival HST data too. By comparing their properties to the ones found for rings in inactive galaxies, the efficiency of star formation in the presence of a low-luminosity AGN could be addressed, ideally complemented by molecular gas data.

ACKNOWLEDGMENTS

We would like to thank the anonymous referee for her/his constructive comments which considerably improved the quality of the paper. This work was supported in part by the German Federal Department for Education And Research (BMBF) under the project numbers 05 AL2VO1/8, 05 AL2EIB/4, 05 AL2EEA/1, 05 AL2PCA/5, 05 AL5VH1/5, 05 AL5PC1/1, and 05 A08VH1. The LBT is an international collaboration among institutions in the United States, Italy, and Germany. LBT Corporation partners are as follows: The University of Arizona on behalf of the Arizona Board of Regents; Istituto Nazionale di Astrofisica, Italy; LBT Beteiligungsgesellschaft, Germany, representing the Max-Planck Society, The Leibniz Institute for Astrophysics Potsdam, and Heidelberg University; The Ohio State University, and The Research Corporation, on behalf of The University of Notre Dame, University of Minnesota and University of Virginia. Open Access funding enabled and organized by Projekt DEAL.

ORCID

J. Heidt https://orcid.org/0000-0002-0320-1292

REFERENCES

Awaki, H., Terashima, Y., Higaki, Y., & Fukazawa, Y. 2009, *PASJ*, *61*, S317.

Barbosa, F. K. B., Storchi-Bergmann, T., Cid Fernandes, R., Winge, C., & Schmitt, H. 2006, *Mon. Not. R. Astron. Soc.*, *371*(1), 170.

Barbosa, F. K. B., Storchi-Bergmann, T., Cid Fernandes, R., Winge, C., & Schmitt, H. 2009, *Mon. Not. R. Astron. Soc.*, *396*(1), 2.

Bournaud, F., Combes, F., & Semelin, B. 2005, *Mon. Not. R. Astron. Soc.*, *364*(1), L18.

Busch, G., Eckart, A., Valencia-, M. S., Fazeli, N., Scharwächter, J., Combes, F., & García-Burillo, S. 2017, *A&A*, *598*, A55.

de Vaucouleurs, G., de Vaucouleurs, A., Corwin, J., Herold, G., Buta, R. J., Paturel, G., & Fouque, P. 1991, Third Reference Catalogue of Bright Galaxies.

Domínguez-Fernández, A. J., Alonso-Herrero, A., García-Burillo, S., et al. 2020, *A&A*, *643*, A127.

Elitzur, M. 2006, *New A Rev.*, *50*(9-10), 728.
Eminian, C., Kauffmann, G., Charlot, S., Wild, V., Bruzual, G., Rettura, A., & Loveday, J. 2008, *Mon. Not. R. Astron. Soc.*, *384*(3), 930.
Erwin, P. 2004, *A&A*, *415*, 941.
Erwin, P., & Sparke, L. S. 2003, *ApJS*, *146*(2), 299.
Esposito, S., Riccardi, A., Pinna, E., et al. 2012, *In Adaptive Optics Systems III*, eds. B. L. Ellerbroek, E. Marchetti & J.-P. Véran, Vol. *8447*, SPIE (Amsterdam, Netherlands), 84470U.
Fazeli, N., Busch, G., Eckart, A., Combes, F., Misquitta, P., & Straubmeier, C. 2020a, *A&A*, *638*, A53.
Fazeli, N., Eckart, A., Busch, G., Yttergren, M., Combes, F., Misquitta, P., & Straubmeier, C. 2020b, *A&A*, *638*, A36.
Ferrarese, L., & Merritt, D. 2000, *ApJ*, *539*(1), L9.
Ferruit, P., Wilson, A. S., & Mulchaey, J. 2000, *ApJS*, *128*(1), 139.
Gebhardt, K., Bender, R., Bower, G., et al. 2000, *ApJ*, *539*(1), L13.
Grudić, M. Y., Hopkins, P. F., Lee, E. J., Murray, N., Faucher-Giguère, C.-A., & Johnson, L. C. 2019, *Mon. Not. R. Astron. Soc.*, *488*(2), 1501.
Gu, Q.-S., Shi, L., Lei, S.-J., Liu, W.-H., & Huang, J.-H. 2003, *Chin. J. Astron. Astrophys.*, *3*, 203.
Häring, N., & Rix, H.-W. 2004, *ApJ*, *604*(2), L89.
Hopkins, P. F., Hernquist, L., Cox, T. J., & Kereš, D. 2008, *ApJS*, *175*(2), 356.
Hopkins, P. F., Murray, N., Quataert, E., & Thompson, T. A. 2010, *Mon. Not. R. Astron. Soc.*, *401*(1), L19.
Hopkins, P. F., & Quataert, E. 2010, *Mon. Not. R. Astron. Soc.*, *407*(3), 1529.
Huchra, J. P., Wyatt, W. F., & Davis, M. 1982, *AJ*, *87*, 1628.
Kim, W.-T., & Elmegreen, B. G. 2017, *ApJ*, *841*(1), L4.
Kormendy, J., Bender, R., & Cornell, M. E. 2011, *Nature*, *469*(7330), 374.
Kuo, C. Y., Braatz, J. A., Condon, J. J., et al. 2011, *ApJ*, *727*(1), 20.
Ma, C., de Grijs, R., & Ho, L. C. 2017, *ApJS*, *230*(2), 14.
Ma, C., de Grijs, R., & Ho, L. C. 2018, *ApJ*, *857*(2), 116.
Ma, J., Maksym, W. P., Fabbiano, G., et al. 2021, *ApJ*, *908*(2), 155.
Malkan, M. A., Gorjian, V., & Tam, R. 1998, *ApJS*, *117*(1), 25.
Marconi, A., & Hunt, L. K. 2003, *ApJ*, *589*(1), L21.
Martini, P., Pogge, R. W., Ravindranath, S., & An, J. H. 2001, *ApJ*, *562*(1), 139.
Martini, P., Regan, M. W., Mulchaey, J. S., & Pogge, R. W. 2003a, *ApJS*, *146*(2), 353.
Martini, P., Regan, M. W., Mulchaey, J. S., & Pogge, R. W. 2003b, *ApJ*, *589*(2), 774.
Möllenhoff, C., & Heidt, J. 2001, *A&A*, *368*, 16.
Moran, E. C., Barth, A. J., Kay, L. E., & Filippenko, A. V. 2000, *ApJ*, *540*(2), L73.
Mulchaey, J. S., Regan, M. W., & Kundu, A. 1997, *ApJS*, *110*(2), 299.
Mundell, C. G., Ferruit, P., Nagar, N., & Wilson, A. S. 2009, *ApJ*, *703*(1), 802.
Nilson, P. 1973, Nova Acta Regiae Soc. Sci. Upsaliensis Ser. V, 0.
Peng, C. Y., Ho, L. C., Impey, C. D., & Rix, H.-W. 2010, *AJ*, *139*(6), 2097.
Persson, S. E., Murphy, D. C., Krzeminski, W., Roth, M., & Rieke, M. J. 1998, *AJ*, *116*(5), 2475.
Schlafly, E. F., & Finkbeiner, D. P. 2011, *ApJ*, *737*(2), 103.
Seifert, W., Appenzeller, I., Baumeister, H., et al. 2003, in: *Instrument Design and Performance for Optical/Infrared Ground-based Telescopes*, eds. M. Iye & A. F. M. Moorwood, Vol. *4841*, SPIE (Waikoloa, Hawaii), 962.
Skrutskie, M. F., Cutri, R. M., Stiening, R., et al. 2003, *VizieR Online Data Catalog*, *VII/233*.
Storchi-Bergmann, T., & Schnorr-Müller, A. 2019, *Nat. Astron.*, *3*, 48.
Theureau, G., Hanski, M. O., Coudreau, N., Hallet, N., & Martin, J. M. 2007, *A&A*, *465*(1), 71.
Thronson, J., Harley, A., & Greenhouse, M. A. 1988, *ApJ*, *327*, 671.
Tody, D. 1986, in: *Instrumentation in Astronomy VI*, ed. D. L. Crawford, Vol. *627*, SPIE (Tucson, Arizona), 733.
van Driel, W., & Buta, R. J. 1991, *A&A*, *245*, 7.
Woo, J.-H., & Urry, C. M. 2002, *ApJ*, *579*(2), 530.

AUTHOR BIOGRAPHY

Leonid Stefan Schey is a master's student at the Faculty of Physics and Astronomy of the Ruprecht-Karls-University in Heidelberg, Germany. He obtained his B.Sc degree in physics in 2021 from the same faculty. His current research focuses on the investigation of modified gravity models and their applicability in cosmology.

How to cite this article: Schey, L., Heidt, J., Pramskiy, A., et al. 2023, *Astron.Nachr.*, *344*, e230094. https://doi.org/10.1002/asna.20230094

APPENDIX A. BEST-FIT RESULTS

The Tables A1–A3 show 52 of the 58 best-fit parameters for each of the bands. We excluded the center coordinates of the three components as they have no real scientific purpose. For the Sérsic profiles derived for the disk, bulge, and the ring, we list the magnitude, effective radius r_e in pixels, the Sérsic index n, the ellipticity q and the position angle θ_{PA}. For the ring, we give in addition the inner and outer truncation break radius r_{break}, the length of the asymptotic function Δr_{soft} and the corresponding amplitudes and phases for the Fourier modes F1–F8 and the bending mode B3. To make the tables as well readable as possible, we list the statistical uncertainties for each parameter based on the covariance matrix of the fit individually below in brackets. See 3.1 for details.

TABLE A1 Best-fit parameters in the J-band.

		– Sérsic –	mag	r_e [*pixel*]	n	q	θ_{PA} [°]
		Fourier	F(mode): ampl. & phase	F(mode): ampl. & phase		F(mode): ampl. & phase	
		Bending	B(mode): amplitude	B(mode): amplitude		B(mode): amplitude	
Component	**#**	**Truncation**	**Inner or outer**	r_{break} [*pixel*]	Δr_{soft} [*pixel*]	q	θ_{PA}[°]
Ring	1	-Sérsic-	13.53	186.70	0.80	1.00	72.03
			…	(1.26)	(0.01)	(0.01)	(0.01)
		Fourier	F1: 1.79, −113.36	F2: 0.81, 65.78		F3: −0.37, 38.05	
			(F1: 0.01, 0.33)	(F2: 0.01, 0.18)		(F3: 0.01, 0.22)	
		Fourier	F4: −0.114, 14.31	F8: −0.042, 18.15		…	
			(F4: 0.001, 0.32)	(F8: 0.001, 0.20)		…	
		Bending	B3: 99.20	…		…	
			(B3: 2.28)	…		…	
	1	Truncation	Inner	152.49	137.69	1.00*	72.03*
			…	(0.47)	(0.64)	(0.01*)	(0.01*)
		Fourier	F1: −0.53, 62.88	F2: 0.46, 81.73		F3: 0.12, 9.88	
			(F1: 0.01, 0.18	(F2: 0.01, 0.06)		(F3: 0.01, 0.07)	
		Fourier	F4: 0.099, 18.16	F8: −0.056, 4.35		…	
			(F4: 0.001, 0.08)	(F8: 0.001, 0.03)		…	
		Bending	B3: −61.60	…		…	
			(B3: 0.38)	…		…	
	1	Truncation	Outer	39.97	134.41	1.00*	72.03*
			…	(0.25)	(0.29)	(0.01*)	(0.01*)
		Fourier	F1: 0.12, −179.51	F2: 0.18, 36.79		F3: 0.13, −57.96	
			(F1: 0.01, 1.31)	(F2: 0.01, 0.29)		(F3: 0.01, 0.11)	
		Fourier	F4: 0.122, 6.57	F8: −0.021, −0.77		…	
			(F4: 0.001, 0.06)	(F8: 0.001, 0.09)		…	
		Bending	B3: −1.01	…		…	
			(B3: 0.01)	…		…	
Disk	2	-Sérsic-	11.31	163.75	1.46	0.72	51.79
			(0.01)	(0.07)	(0.01)	(0.01)	(0.02)
Bulge	3	-Sérsic-	16.95	12.54	0.44	0.74	2.16
			(0.01)	(0.03)	(0.01)	(0.01)	(0.45)
J–Merit	$\chi^2_{\nu,cor} = 1.632$			$N_{dof} = 361143$			

TABLE A2 Best-fit parameters in the H-band.

		– Sérsic –	mag	r_e [*pixel*]	n	q	θ_{PA} [°]
		Fourier	F(mode): ampl. & phase	F(mode): ampl. & phase		F(mode): ampl. & phase	
		Bending	B(mode): amplitude	B(mode): amplitude		B(mode): amplitude	
Component	**#**	**Truncation**	**Inner or outer**	r_{break} [*pixel*]	Δr_{soft} [*pixel*]	q	θ_{PA}[°]
Ring	1	-Sérsic-	12.79	189.10	1.23	0.97	69.51
			…	(2.76)	(0.01)	(0.01)	(0.02)
		Fourier	F1: 0.54, −99.93	F2: 1.01, 54.77		F3: −0.09, −32.71	
			(F1: 0.01, 0.4)	(F2: 0.01, 0.15)		(F3: 0.01, 0.62)	
		Fourier	F4: 0.395, 43.51	F8: −0.006, 0.91		…	
			(F4: 0.001, 0.16)	(F8: 0.001, 1.03)		…	
		Bending	B3: 54.9	…		…	
			(B3: 1.61)	…		…	
	1	Truncation	Inner	138.15	121.15	0.97*	69.51*
			…	(0.38)	(0.51)	(0.01*)	(0.02*)
		Fourier	F1: −0.29, 76.38	F2: 0.39, 77.09		F3: 0.10, 21.77	
			(F1: 0.01, 0.25)	(F2: 0.01, 0.07)		(F3: 0.01, 0.12)	
		Fourier	F4: 0.105, 30.98	F8: −0.061, 8.86		…	
			(F4: 0.001, 0.10)	(F8: 0.001, 0.03)		…	
		Bending	B3: −11.40	…		…	
			(B3: 0.24)	…		…	
	1	Truncation	Outer	56.87	104.42	0.97*	69.51*
			…	(0.15)	(0.24)	(0.01*)	(0.02*)
		Fourier	F1: 0.24, −149.50	F2: 0.21, 47.78		F3: 0.09, −47.18	
			(F1: 0.01, 0.24)	(F2: 0.01, 0.14)		(F3: 0.01, 0.17)	
		Fourier	F4: 0.102, 7.06	F8: −0.013, −4.50		…	
			(F4: 0.001, 0.12)	(F8: 0.001, 0.14)		…	
		Bending	B3: −2.40	…		…	
			(B3: 0.01)	…		…	
Disk	2	-Sérsic-	10.22	197.89	1.79	0.72	49.73
			(0.01)	(0.07)	(0.01)	(0.01)	(0.02)
Bulge	3	-Sérsic-	15.26	13.89	0.76	0.80	-27.23
			(0.01)	(0.03)	(0.01)	(0.01)	(0.29)
H–Merit	$\chi^2_{\nu,cor} = 1.508$			$N_{dof} = 361143$			

TABLE A3 Best-fit parameters in the Ks-band.

		– Sérsic –	mag	r_e [*pixel*]	n	q	θ_{PA} [°]
		Fourier	F(mode): ampl. & phase	F(mode): ampl. & phase		F(mode): ampl. & phase	
		Bending	B(mode): amplitude	B(mode): amplitude		B(mode): amplitude	
Component	**#**	**Truncation**	**Inner or outer**	r_{break} [*pixel*]	Δr_{soft} [*pixel*]	q	θ_{PA}[°]
Ring	1	-Sérsic-	12.38	107.29	0.85	1.00	69.12
			…	(0.79)	(0.01)	(0.01)	(0.03)
		Fourier	F1: 0.76, −130.46	F2: 0.95, 42.58		F3: −0.23, 19.17	
			(F1: 0.01, 0.25)	(F2: 0.01, 0.09)		(F3: 0.01, 0.17)	
		Fourier	F4: −0.185, −14.81	F8: 0.078, −1.20		…	
			(F4: 0.003, 0.18)	(F8: 0.001, 0.07)		…	
		Bending	B3: −0.71	…		…	
			(B3: 0.08)	…		…	
	1	Truncation	Inner	122.01	101.07	1.00*	69.12*
			…	(0.25)	(0.37)	(0.01*)	(0.03*)
		Fourier	F1: −0.22, 53.78	F2: 0.28, 79.11		F3: 0.016, −19.42	
			(F1: 0.01, 0.33)	(F2: 0.01, 0.12)		(F3: 0.001, 1.43)	
		Fourier	F4: 0.085, 33.10	F8: −0.049, 14.37		…	
			(F4: 0.001, 0.12)	(F8: 0.001, 0.04)		…	
		Bending	B3: 14.64	…		…	
			(B3: 0.14)	…		…	
	1	Truncation	Outer	60.37	148.29	1.00*	69.12*
			…	(0.31)	(0.79)	(0.01*)	(0.03*)
		Fourier	F1: −0.30, −144.46	F2: −0.24, 4.88		F3: 0.16, 33.83	
			(F1: 0.01, 0.22)	(F2: 0.01, 0.44)		(F3: 0.01, 0.10)	
		Fourier	F4: 0.133, −1.12	F8: −0.022, −1.47		…	
			(F4: 0.002, 0.10)	(F8: 0.001, 0.13)		…	
		Bending	B3: −2.00	…		…	
			(B3: 0.02)	…		…	
Disk	2	-Sérsic-	10.09	157.33	1.61	0.71	49.58
			(0.01)	(0.04)	(0.01)	(0.01)	(0.02)
Bulge	3	-Sérsic-	13.22	15.97	1.04	0.89	-18.59
			(0.01)	(0.02)	(0.01)	(0.01)	(0.18)
Ks–Merit	$\chi^2_{\nu,cor} = 1.275$			$N_{dof} = 361143$			